Special Issue
Martensitic and Bainitic Transformations in Steels; Fundamentals and Their Applications

ISIJ International, Vol. 64 (2024), No. 2, pp. 257–267
https://doi.org/10.2355/isijinternational.ISIJINT-2023-228

Thermodynamic Analysis of the Formation Mechanism of Metastable Carbides during Tempering of Fe–C Martensite

Masanori ENOKI,[1)]* Yu SATO[2)] and Hiroshi OHTANI[3)]

1) Faculty of Materials for Energy, Shimane University, 1060 Nishikawatsucho, Matsue, Shimane, 690-8504 Japan.
2) Western Digital GK, 6-6 Kitakami Kogyodanchi, Kitakami, Iwate, 024-8555 Japan.
3) Toyota Physical and Chemical Research Institute, 41-1, Yokomichi, Nagakute, Aichi, 480-1192 Japan.

(*Received June 4, 2023; Accepted August 22, 2023; Published January 30, 2024*)

A thermodynamics analysis based on first-principles calculations was used to establish the behavior of carbon in the matrix during the preliminary stage of the tempering process of steel, as well as the formation mechanism of the η-carbide and cementite phases. Models were constructed in which carbon occupied three octahedral interstitial sites in BCC-Fe, and the cluster expansion and variation method was applied to evaluate the free energy of forming the solid solution. Furthermore, the thermal equilibrium distribution of carbon was obtained using the Monte Carlo simulation method by using the effective cluster interactions. The variable-cell nudged elastic band method was applied to evaluate the energy barrier that exists in the transition process. In addition, transition models considering the influence of interfaces were constructed. The Monte Carlo simulations of BCC-Fe showed well-defined clustering of carbon atoms. Furthermore, the free energies calculated from the cluster expansion and variation method showed two-phase separations between Fe and Fe_2C, suggesting that these clusters are formed by two-phase separation based on atomic ordering. The energies of the transition processes to η-carbide and cementite were calculated from the structural models created based on these local structural findings. By comparing the energy barriers in each transition process, it is shown here that the metastable carbides may occur because of a series of following processes: η-carbide precipitates preferentially in the initial stage of tempering; consequently, cementite precipitates in the third stage using the η-carbides as precipitation sites, and finally, η-carbide transitions to cementite.

KEY WORDS: first-principles calculations; thermodynamics analysis; carbides; clustering; precipitation; solid solution.

1. Introduction

Martensitic transformation is caused by a shear deformation without the diffusion of atoms.[1,2)] Although it is possible to obtain a very hard structure in steels via this transformation, the toughness of the resultant material is generally insufficient for use as practical structural materials. Therefore, the material is used after adjusting a balance of strength and toughness by the heat treatment process called tempering. In the course of this process, various metastable carbides form with a temperature change. Because the dispersion in microstructure significantly affects the strength of the material, detailed studies concerning this phenomenon have been undertaken. In particular, the precipitation of cementite (θ-carbide) is one of the causes of low-temperature embrittlement,[3)] and observations of this carbide,[4–15)] as well as ε- and η-carbides, have been widely undertaken by electron beam diffraction. Based on these experimental observations, it is hypothesized that the tempering process can be separated into the following four stages: the preliminary, 1st, 2nd, and 3rd stages.[4,16)]

In the preliminary stage, the microstructure is maintained by heat treatment below 100°C. An initial step of the first stage is aging up to temperatures of approximately 100°C, and it is suggested that the clustering of dissolved carbon occurs in the matrix phase in the temperature range from 100°C to 200°C, resulting in a locally high-carbon region in which the metastable carbide with $Fe_{2–3}C$ composition is formed.[8–11)] The metastable carbides have been reported as two types of carbides: hexagonal ε-carbide and orthorhombic η-carbide.[12,13)] In the first stage, aside from the report that the ε-carbide was generated as a metastable carbide,[14)] another study showed that both ε-carbide and η-carbides formed simultaneously.[15)] Thus, the detail of the transition behavior in this stage has not been fully understood to date. The second step of the tempering process occurs

* Corresponding author: E-mail: masanori.enoki@mat.shimane-u.ac.jp

in the temperature range from 200°C to 300°C, where the residual austenite decomposes into cementite and ferrite. The third stage of the tempering process occurs between 300°C and 500°C, where the metastable carbide formed in the first stage disappears, and the more stable cementite Fe_3C forms followed by the metastable $Fe_{2n+1}C_n$ as well as Fe_5C_2, known as χ-carbide. Because these precipitates in the early aging stage are very fine, it is difficult to clarify the precipitation process by experimental observation; however, recent improvements in analytical techniques have led to discussions of the transition to carbides with local clustering as a precursor.[11,17)]

In this paper, a thermodynamic analysis based on the first-principles calculations was performed, and the tempering process was examined considering clustering behavior in a parent phase. We attempt to elucidate a formation mechanism of the metastable carbides present in the tempering process, such as η-carbide and cementite. Note that in this study, χ-carbide with complex crystal structure and ε-carbide with non-stoichiometric carbide, were excluded from the object due to computational difficulties.

2. Calculation Procedures

2.1. Structure of Martensite

Figure 1 shows the crystallographic structure of body-centered cubic (BCC) Fe and the location of the octahedral interstitial sites. Positions indicated by the symbols □, △, and × are octahedral interstitial sites, and all of these sites are equivalent to each other in the BCC structure. These positions are referred to as the a-sites, b-sites, and c-sites, respectively. The axial ratio of martensite is induced because of a bias in this site occupation that originates from the crystallographic structural correspondence between face-centered cubic (FCC) and BCC in martensitic transformation. In FCC/BCC structures, a lattice correspondence called the Bain correspondence,[18)] shown in **Fig. 2**, exists. Thus, the a-sites, b-sites, and c-sites in the BCC structure are not equivalent in the FCC structure, and any one of these can correspond to the octahedral interstitial position in the FCC structure. Therefore, when the diffusionless transformation occurs, the transition to the BCC lattice occurs retaining only the carbon atoms dissolved in any one set of these sites. Therefore, in the martensitic transformation, the BCC structure is formed in which carbon is dissolved only in any one of these positions. This dissolved carbon causes uniaxial strain by increasing the distance between its first nearest neighboring Fe atoms. Below 0.25 at.%C, however, such a body-centered tetragonal (BCT) structure has not been observed. This is attributed to a short-range diffusion of carbon over the length scale of a single atomic spacing. That is, the BCT structure becomes cubic because the dissolved carbon can be distributed across the equivalent interstitial positions via short-range diffusion.[19)] From the presented crystallographic findings, it is understood that the uniaxial elongation is eliminated and the BCT structure transitions to the BCC structure during the tempering process through the migration of carbon.

A previous report[20)] described the BCT solid solutions using the first-principles calculations and pointed out that BCT-Fe_2C ordered structures in the BCT structure could transform to η-carbide. However, that study used a model in which carbon occupies only the c-site, and the effect of carbon occupancy on the a- and b-sites was not discussed. In actuality, if the tetragonal strain is small, carbon is more likely to occupy the a and b sites as well. Such regions appear frequently in the martensite structure with low carbon content, such as in the surrounding matrix after the precipitation of high-carbon carbides.

In the present study, we performed new calculations using BCC-Fe as the structure model with negligibly small tetragonal strain for the discussion about the carbide precipitation process when the a- and b-sites are occupied as well as c-sites.

2.2. Cluster Expansion-Cluster Variation Method

In this study, the cluster expansion and cluster variation method (CE-CVM) was used to evaluate the free energy of formation for martensite. The cluster expansion method is a technique that expresses the enthalpy of formation of an ordered structure as the sum of a product of the effective cluster interaction energies (ECIs) and the correlation function corresponding to the cluster density, assuming the ordered structure is to be formed from various kinds of clusters. In this method, the total energy, $E^{\phi}(V)$, of an ordered structure, ϕ, in a volume, V, is expressed as

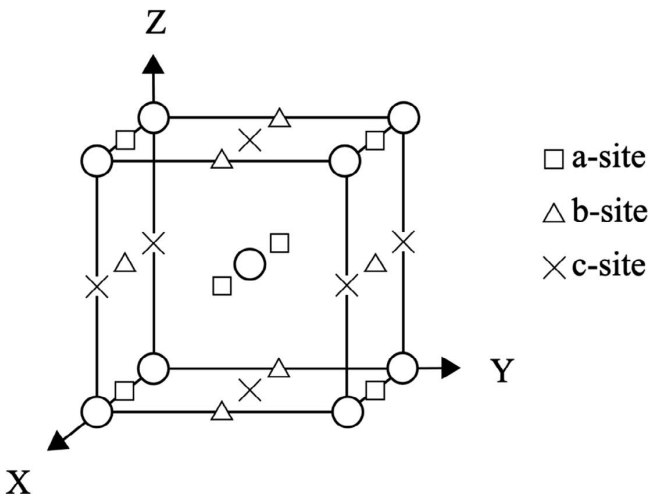

Fig. 1. Crystallographic structure of BCC-Fe and the location of the three considered octahedral interstitial sites.

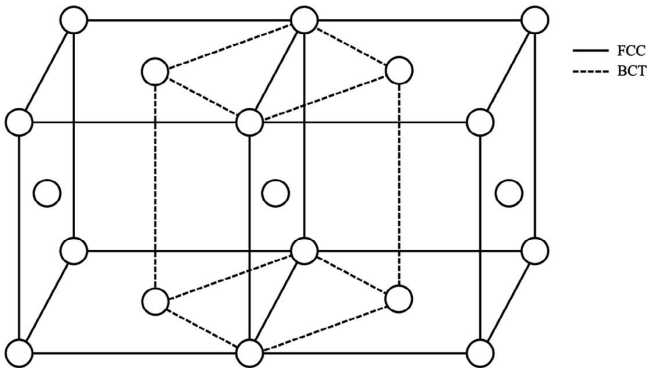

Fig. 2. Crystallographic structural correspondence between face-centered cubic (FCC) and body-centered tetragonal (BCT).

$$E^{\phi}(V) = \sum_{\alpha}^{\alpha_{\max}} J_{\alpha}(V) \cdot \xi_{\alpha}, \quad \text{..... (1)}$$

where $J_\alpha(V)$ represents the ECIs in that volume and ζ_α represents the correlation function of the cluster of indexed by α. Using an infinite number of clusters, the total energy given by Eq. (1) can be accurately determined, but for practical calculations, the calculation must be terminated with a finite number of clusters. Therefore, defining a maximum cluster ($\alpha_{\max}$) that specifies an upper bound on size, the energy of the ordered structure is calculated by the sum of the energies of subclusters that are included in the $\alpha_{\max}$. The cluster correlation function (ζ_α) is defined by an array of occupied spin operators (σ) on crystal lattice points indexed by i,

$$\xi_{\alpha} = \frac{1}{N(n)} \sum_{i_1}^{N} \sum_{i_2}^{N} \cdots \sum_{i_n}^{N} \sigma(i_1)\sigma(i_2)\cdots\sigma(i_n). \quad \text{..... (2)}$$

In Eq. (2), n is the number of vertices in the cluster of α and N is the number of sites in the crystal structure. Because a combination of correlation functions can be uniquely determined for any perfectly ordered structure, the cluster concentration and the correlation function have a one-to-one relationship. The total energy, $E^{\phi}(V)$, of an ordered structure, ϕ, can be accurately evaluated using first-principles calculations; the unknown ECIs, J_α, can then be obtained using Eq. (1). However, in this method, the ECIs that completely reproduce the left-hand side of Eq. (1) cannot be obtained because the actual computation is terminated at a finite cluster size $\alpha_{\max}$. Here, we calculate energies of ordered structures sufficiently large compared with the number of subclusters and determine the ECIs that can reproduce the difference between the left- and right-hand sides of Eq. (1) using the least squares method. Once the ECIs have been determined, the energies of any atomic arrangement can be obtained within the accuracy of the cluster expansion without using first-principles calculations. Furthermore, by considering the entropy of a given cluster arrangement, the free energy of the structure at temperature (T) can be expressed as

$$F(T;V) = \sum_{\alpha}^{\alpha_{\max}} J_{\alpha}(V) \cdot \xi_{\alpha} - T \sum_{\alpha}^{\alpha_{\max}} \gamma_{\alpha} \cdot S_{\alpha}, \quad \text{..... (3)}$$

where $\gamma_\alpha \cdot S_\alpha$ is the contribution to the entropy from clusters α obtained using the Kikuchi–Barker factor.[21] The free energy can then be calculated by applying the variational method to Eq. (3) and obtaining a correlation function that minimizes the value of $F(T;V)$.

In this study, the projector-augmented wave method was used to evaluate the value of $E^{\phi}(V)$ using the first-principles computational code Vienna Ab initio Simulation Package.[22,23] The generalized gradient approximation was used to calculate the interchange correlation term, and the energy cutoff for the plane wave was taken to be 400 eV. iCVM code was used for CE-CVM calculations.[24]

2.2.1. Ordered BCC Structures

This section describes the details of the method to generate the order structure data for the BCC structures used in the cluster expansion method. About 500 models with the sublattice model of $Fe_4(C,Vac)_{12}$ were constructed, and the structural relaxation based on first-principles calculations was applied. However, some of these structures deviated significantly from BCC because of the small minimum distance between the Fe and C atoms of the first nearest neighbor pair. The cluster expansion method using all of these structures results in unacceptably high errors of 500 meV/site.

Thus, in the present study, a screening of appropriate structure models was conducted. We used an energy–volume (E–V) curve calculation to screen for structures. The specific procedure used in this process was as follows:

① The BCC-Fe lattice is fixed, and carbon atoms and vacancies are considered at octahedral positions.
② Multiple structure models with different volumes are prepared, and the energies are evaluated after relaxing only the local atomic positions of each structural model under volume-fixed conditions.
③ E–V curve is created and regressed with the Murnaghan equation of state.[25]
④ Structure models with large root-mean-square error (> 0.1 eV) are excluded.
⑤ The energy at the most stable volume of the selected structures is used for the cluster expansion.

In the calculations process of ②, it is often observed that atom positions deviating significantly from the BCC structure do not exhibit systematic positional relaxation across different volumes. As a result, the obtained E–V curves deviate from the Murnaghan equation. To eliminate data contamination caused by these structures, they were removed from the analysis. By applying this procedure, the error in the cluster expansion was successfully reduced to 40 meV/site.

2.3. Monte Carlo Simulations

To confirm the clustering behavior of carbon during the tempering process, the Markov chain Monte Carlo method was used. In this method, the thermal equilibrium distribution of atoms was obtained using the ECIs determined from the cluster expansion method.

The Monte Carlo simulation uses the BCC-type supercell made up of 20 unit cells in each axis direction. Periodic boundary condition was applied at the boundaries of the cells. In the supercell, 16 000 iron atoms at the lattice points were considered as well as 48 000 octahedral interstitial positions. A process of exchanging atomic positions of all carbon atoms and vacancies at the octahedral interstitial positions was taken as a single Monte Carlo step (MCS), and the canonical ensemble was constructed by performing computations of up to 1 000 MCSs. The initial states were prepared as a supercell in which carbon atoms were placed randomly in the octahedral interstitial positions at 5 at.%. The temperatures considered were at 50 K intervals between 350 K and 600 K, and this range covers the tempering process from the initial to the third stage. All calculations were performed under constant volume conditions.

2.4. Variable-Cell Nudged Elastic Band Method

When a substance transitions from one state to another, a change in the energy because of the transition takes place along the minimum energy path (MEP). The highest energy point of this path is taken at the saddle point. The activation energy barrier is calculated from the energy difference

between the initial state and the saddle point. The nudged elastic band (NEB) method can be used to determine the MEP and the saddle point from the start and the end points of the transition process for a given composition. In this method, we first create an N+1 structure image ($\mathbf{R}_0$, $\mathbf{R}_1$, …, $\mathbf{R}_N$) linking the start point and the end point of the process. Here, $\mathbf{R}_0$ and $\mathbf{R}_N$ are crystal structure images of the start point and the end point of the transition. Each structure image is regarded as a phase point on the transition path, and we consider a spring that connects these images on the energy surface. The force F_i^{NEB} acting at the point $\mathbf{R}_i$ is defined as

$$F_i^{\mathrm{NEB}} = F_i^{\nabla\perp} + F_i^{\mathrm{S}\parallel}, \quad \text{..... (4)}$$

where $F_i^{\nabla\perp}$ is the normal component of the force from the potential gradient relative to the path and $F_i^{\mathrm{S}\parallel}$ is the parallel component of the force received from a spring relative to the transition path. Considering the unit vector $\hat{\tau}_i$ of the tangent to the transition path at the phase point $\mathbf{R}_i$, $F_i^{\nabla\perp}$ and $F_i^{\mathrm{S}\parallel}$ can be expressed as

$$F_i^{\nabla\perp} = F_i^{\nabla} - \left(F_i^{\nabla}\cdot\hat{\tau}_i\right)\hat{\tau}_i, \quad \text{..... (5)}$$

$$F_i^{\mathrm{S}\parallel} = k\left(\left|\mathbf{R}_{i+1}-\mathbf{R}_i\right| - \left|\mathbf{R}_i-\mathbf{R}_{i-1}\right|\right)\hat{\tau}_i, \quad \text{..... (6)}$$

where F_i^{∇} is a potential force at $\mathbf{R}_i$ because of the energy surface and k is a hypothetical spring constant. In the NEB method, the MEP is obtained by optimizing the structure of each phase such that F_i^{NEB} is minimized for all phases. However, because the lattice shapes of the unit cell are calculated under the condition of invariance in the conventional NEB method, it is not possible to consider a transition process including the lattice deformation as a degree of freedom. Therefore, following the work of Qian *et al.*,[26] we used the technique referred to as the variable-cell NEB (VC-NEB) method. The conventional NEB method proceeds considering the energy surface, whereas the VC-NEB method introduces a finite strain tensor that allows for the energy surface to be extended to an enthalpy surface; this method was then used to carry out the calculation. In this study, the MEPs of the phase transformation were obtained using the VC-NEB method, which was implemented in the Universal Structure Predictor: Evolutionary Xtallography code (USPEX).[27,28]

For the calculations, 11 initial images were created by the linear interpolation from the initial structure to the final structure. The distance between those images was defined from the sum of the displacements of all atomic positions, and new interpolated image was added in the calculation if the distance between the images was greater than the defined threshold. The threshold was given as the average distance between the initial images.

3. Calculation Results

3.1. Free Energy of the Fe–C Binary System

The formation free energy of the Fe–C binary system up to 50 at.%C at 350 K calculated using the CE-CVM is shown in **Fig. 3**. The figure shows that for higher carbon concentration, the free energy is increased, which is considered to be because of energetical destabilization by a supersaturated solid solution of carbon. Furthermore, in the concentration range of 0–33 at.%C (*i.e.*, Fe–Fe_2C), the second derivative of the carbon concentration of the free energy of formation is negative. This indicates that there is a two-phase separation between higher and lower composition regions. Because a metastable ground state ($P4_2/mnm$) was identified in Fe_2C from the ordered structures created by the cluster expansion method, it is expected that the ordering of the $P4_2/mnm$ structure is a candidate for the origin of the two-phase separation. Such two-phase separation has also been confirmed in a previous study[20] investigating the BCT structure model. It can thus be inferred that such a two-phase separation is one of the thermodynamic origins of the carbon clustering that is observed during the early stages of tempering.

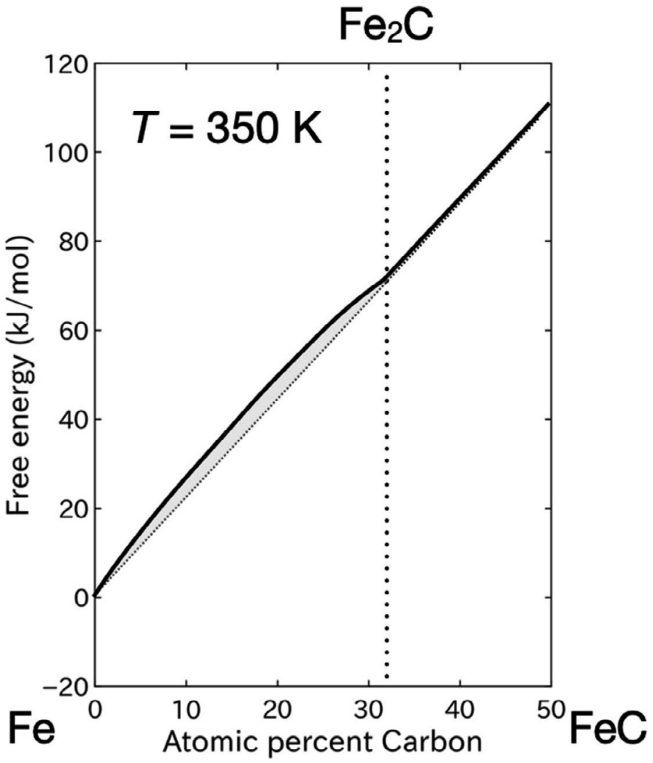

Fig. 3. Formation free energy of the Fe–C binary system for a temperature of 350 K calculated using the CE-CVM. There is a two-phase separation between higher and lower carbon concentrations.

3.2. Atomic Arrangement of Carbon in BCC-Fe

The change in the configuration of the carbon atoms with increasing MCSs at 350 K is shown in **Fig. 4**. As the number of MCSs increases, the carbon-enriched clusters gradually develop. In Fig. 4, an enlarged view of one of the clustered regions is also shown. The figure also displays carbon–carbon bonds at distances of about 2.8 Å. In small clusters, two carbon atoms are locally aligned in the $<001>_{\mathrm{BCC}}$ direction at this distance. In larger clusters, carbon atoms consisting of several atoms were observed to be aligned in the $<001>_{\mathrm{BCC}}$ direction. These features were observed similarly over the temperature range of 50 K to 600 K.

The characteristics of the atomic arrangement of carbon atom clusters are shown in **Fig. 5**. The small spheres in the figure represent carbon/vacancy sites, and circled sites are occupied by carbon. The dotted lines between carbons correspond to the bonds between carbons shown in Fig.

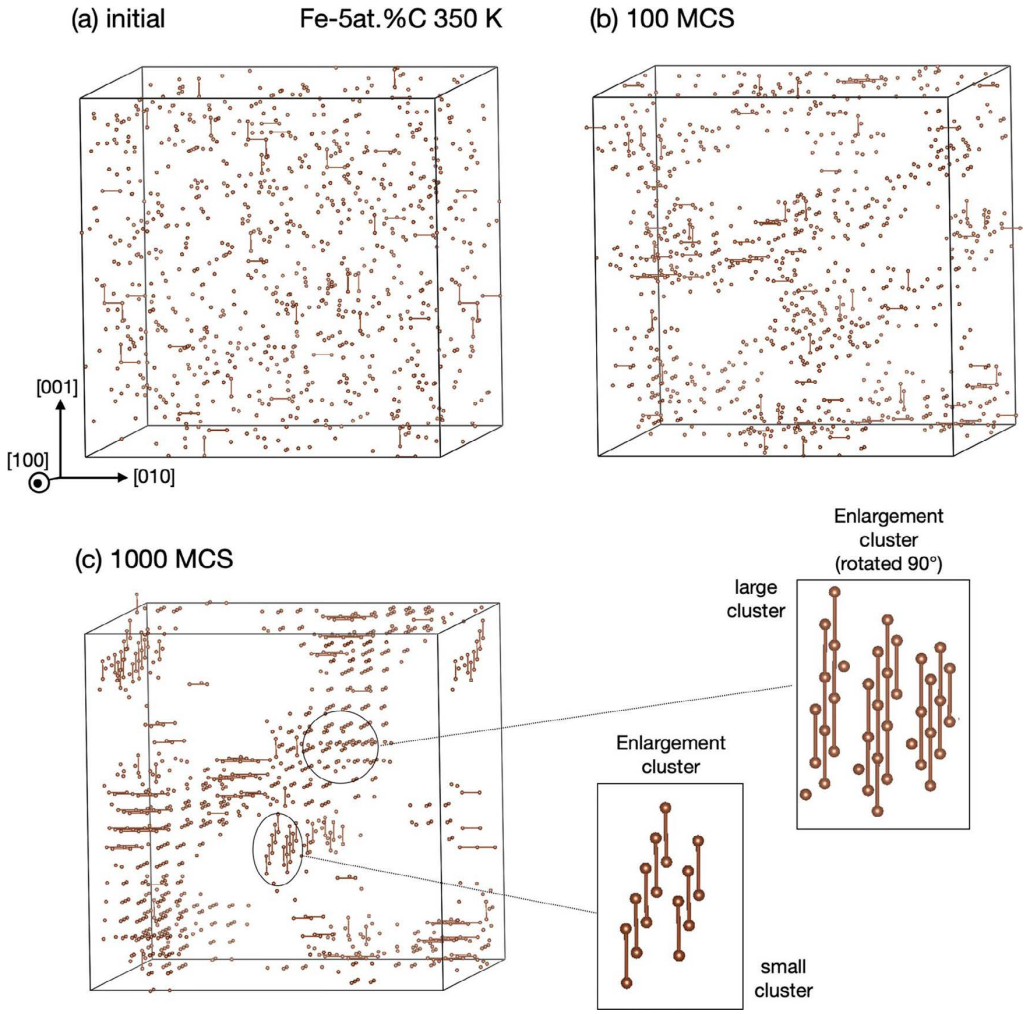

Fig. 4. Changes in a configuration of carbon atoms with increasing Monte Carlo steps (MCSs) at T = 350 K for 5 at.%C. Fe atoms are erased and only carbon atoms are shown. The carbon–carbon bonds in the third nearest neighbor are displayed by the short solid lines in the figure. (Online version in color.)

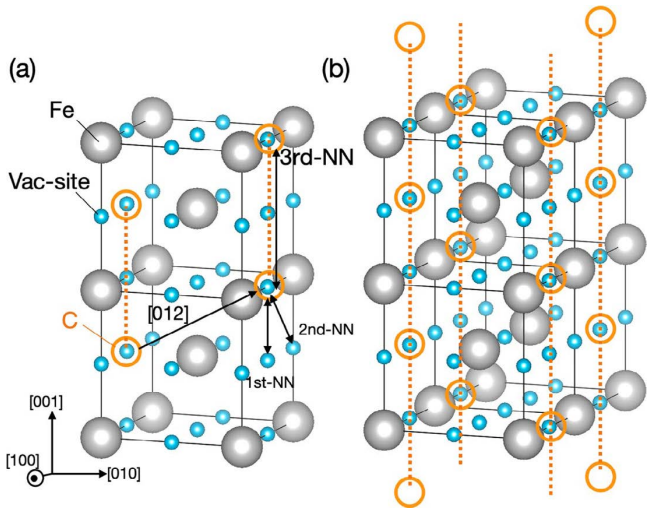

Fig. 5. Details of the crystal structure in clustered regions of carbon. Visualization of characteristics in regions where (a) cluster size is small and (b) cluster size is large. The sites occupied by carbon are indicated by circles. (Online version in color.)

4. The figure shows an example of carbon aligned in the $[001]_{BCC}$ direction, but because of the cubic symmetry, the Monte Carlo calculation confirmed the atomic arrangement of equivalent clusters in the three axes of $<001>_{BCC}$ at the same time. Figure 5(a) shows the arrangement of clusters consisting of carbon pairs identified in the smaller clusters. The carbons occupy a vacancy site corresponding to the third nearest neighbor from carbon atom (~2.8 Å) in the $[001]_{BCC}$ direction. In contrast, the vacancy sites at the first nearest neighbor (~1.4 Å) and second nearest neighbor (~2.0 Å) from carbon are not occupied by carbon, suggesting a tendency to have repulsive interactions between carbon atoms at these distances in BCC-Fe. Furthermore, the carbon pairs tend to be arranged orderly and be aligned in the [012] or [102] shifted position. Figure 5(b) shows the atomic arrangement of the carbon atoms in the large clusters. The local structural features are identical to those in Fig. 5(a), but the one-dimensional arrangement of the carbon atoms increases with increasing size. The three-dimensional arrangement is also well defined, and when constructed to satisfy the periodic boundary condition based on this arrangement, we obtain a Fe_2C structure with $P4_2/mnm$, which is consistent with the metastable basis described in Section 3.1. This suggests that the carbon concentration increases up to Fe_2C because of the development of clusters by the two-phase separation. Because this Fe_2C has the same composition as η-carbide, a structural transformation to η-carbide is assumed. Therefore, this structure

was introduced into the VC-NEB calculations.

On the other hand, a structure consisting of carbon pairs was observed in the region of small clusters, and it is considered that the structure reaches Fe_2C with a gradual increase in carbon concentration. Because the carbon enrichment process to Fe_2C from Fe also involves Fe_3C composition, cementite precipitation is assumed to occur in the intermediate stage of the enrichment process. Hence, we created a Fe_3C structure ($P2_1/c$) by replacing some of the carbon in Fe_2C $P4_2/mnm$ with vacancies and used it in the VC-NEB calculation to determine the transition process from η-carbide to cementite. The details of the structure are described in Section 3.3.1.

3.3. Calculation of Transition Barriers

3.3.1. Transition Models

To calculate the transition barriers using the VC-NEB method, it is necessary to construct a transition model considering a correspondence between the atomic positions in the structure before and after the transition.

In the first stage of tempering, the transition from the BCC-Fe structure to η-carbide occurs. In the third stage of tempering, the transition from BCC-Fe to cementite structure or from η-carbide to cementite structure occurs. Therefore, η-carbide and θ-carbide were used as the final states of the phase transition. The structural parameters of the η-carbide are the space group *Pnnm* with lattice constants a = 4.70 Å, b = 4.32 Å, c = 2.83 Å. On the other hand, the θ-carbide of the space group is *Pnma* and the lattice constants are a = 4.38 Å, b = 5.01 Å, c = 6.69 Å.

To obtain an atomic correspondence between the BCC-Fe and η-carbide structures, a transition model was created based on the orientation relationship ($[100]_\eta//[1\text{–}10]_{BCC}$, $[010]_\eta//[110]_{BCC}$, $[001]_\eta//[001]_{BCC}$) obtained by Jack.[8,29,30] Regarding the BCC-Fe and cementite structures, several orientation relationships have been found.[11,31–35] These appear in different orientations depending on composition, temperature, and cementite precipitation size. In this study, we did not construct the models from all of these patterns and perform a comprehensive calculation. The present study focuses on the model according to Bagaryatsky's orientation relationship,[34,35] *i.e.*, $[100]_\theta//[1\text{–}10]_{BCC}$, $[010]_\theta//[111]_{BCC}$, $[001]_\theta//[11\text{–}2]_{BCC}$. The relationship shows a relatively good correspondence between clustered local structure and atomic positions based on the Monte Carlo simulations.

On the other hand, the orientation relationship between η-carbide and cementite is not clear. Therefore, in this study, we estimated the orientation relationship by combining Jack's and Bagaryatsky's orientation relations. That is, the matrix correspondence is expressed as follows.

$$\begin{pmatrix} 1 & -1 & 0 \\ 1 & 1 & 1 \\ 1 & 1 & -2 \end{pmatrix} = \begin{pmatrix} 1 & 0 & 0 \\ 0 & 1 & 1 \\ 0 & 1 & -2 \end{pmatrix} \begin{pmatrix} 1 & -1 & 0 \\ 1 & 1 & 0 \\ 0 & 0 & 1 \end{pmatrix} \quad \text{..... (7)}$$

Here, the matrix on the left side is the three components of Jack's BCC orientation, and the second matrix on the right side of the equation is the three components of Bagaryatsky's BCC orientation. From this, we assume that the orientation relationships are $[100]_\theta//[100]_\eta$, $[010]_\theta//[011]_\eta$, and $[001]_\theta//[01\text{–}2]_\eta$.

These orientation relationships are summarized in **Figs. 6** and **7**. Figure 6 visualizes the orientation relationship between η and BCC-Fe based on Jack's orientation relationship, while Fig. 7 shows the orientation relationship between cementite and BCC-Fe based on Bagaryatsky's orientation relationship. The relationship in Eq. (7) was also applied to η-carbide in Fig. 7. The orientation relationships between η-carbide and BCC are shown in Figs. 6(a) and 6(b), and Figs. 7(a) and 7(b) show the orientation relationship between cementite and BCC-Fe. In addition, the habit planes are shown in gray colors in the figures.

Note that in VC-NEB calculations, the number of carbon atoms, as well as the orientation relationship, must also match the initial and final structures. In terms of the number of carbon and iron atoms, BCC-Fe_2C in Fig. 6(c) corresponds to η-carbide. Besides, BCC-Fe_3C and η-type-Fe_3C in Figs. 7(c) and 7(e) correspond to cementite. The η-type-Fe_3C is formed by removing carbon from η-Fe_2C. These structures are based on the atomic arrangements in the local structures obtained from the Monte Carlo calculations described in Section 3.2. Figure 6(c) shows a structural model of the long-range ordered structure of Fe_2C sliced by Bagaryatsky's orientation relation. On the other hand, the structure of BCC-Fe_3C is shown in Fig. 7(c), where the carbon atoms replaced with vacancies in BCC-Fe_2C are indicated by shaded symbols and arrows. Because the carbon–carbon pairs exist as shown by the dotted lines, this structure reproduces the local atomic arrangement observed in the Monte Carlo calculation shown in Fig. 5(a). Furthermore, the η-Fe_2C structure and BCC-Fe_2C have high similarity by comparing Figs. 6(a) and 6(c) and Figs. 7(c)

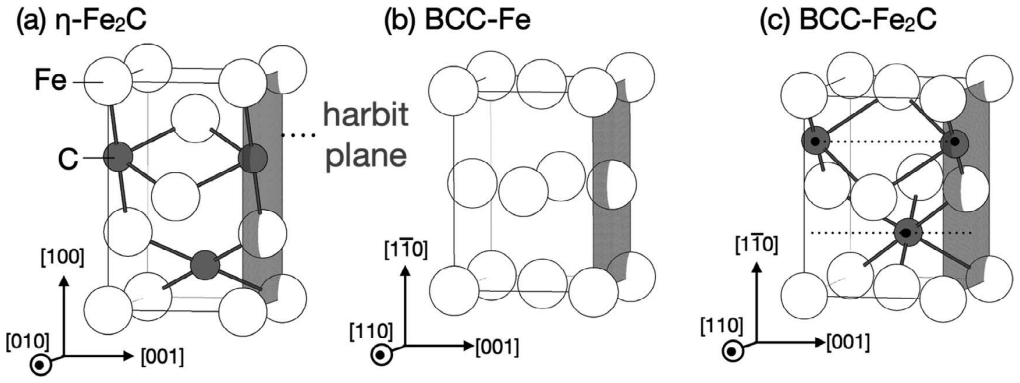

Fig. 6. Orientation relationship between (a) η-carbide and (b, c) BCC-Fe.

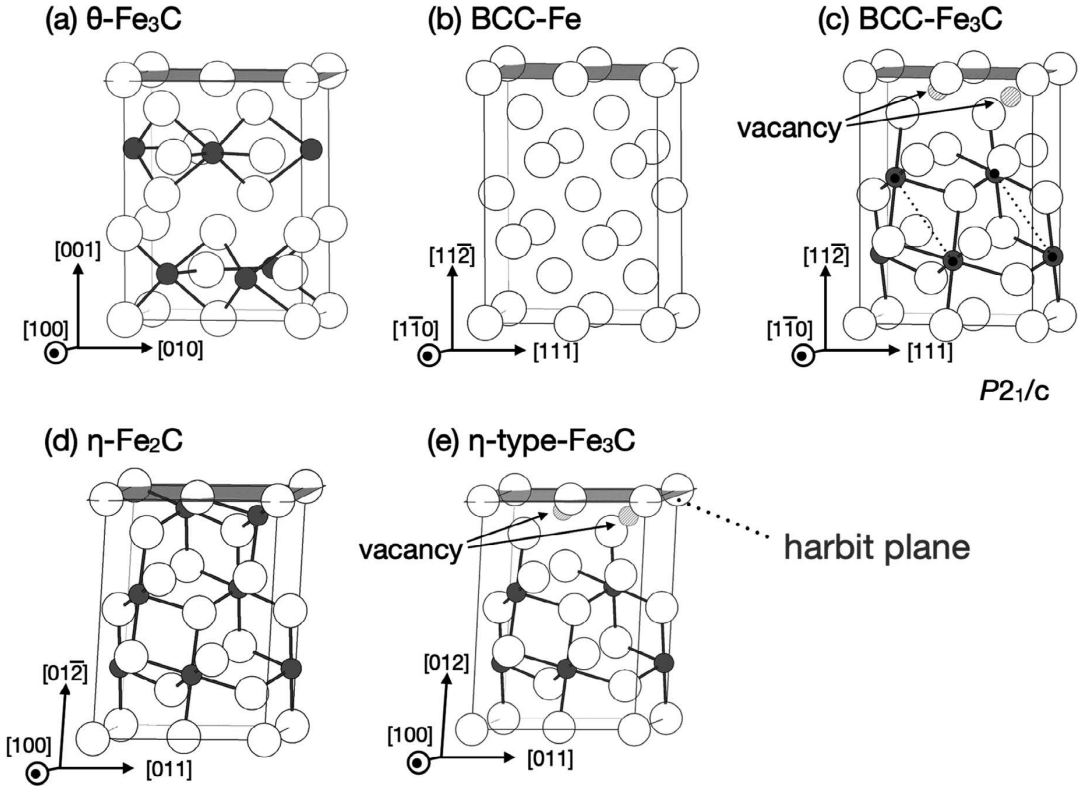

Fig. 7. Orientation relationship between (a) cementite, (b, c) (BCC)-Fe, and (d, e) η-carbide.

and 7(d), and the atomic positions of iron and carbon in the two structures are close. Based on this correspondence, the η-type-Fe_3C structure was created by introducing vacancies at carbon atom positions similar to those in Fig. 7(c). The structure of η-type-Fe_3C is shown in Fig. 7(e). Previous experimental findings do not suggest the existence of such a carbon-deficient structure from η-Fe_2C, but at the interface between η-Fe_2C and matrix, the migration of C atoms can occur constantly via a thermally activated process. This suggests the possibility that such a structure could be locally developed. The transition from BCC-Fe_2C to η-carbide was then calculated using Figs. 6(c) and 6(a), from BCC-Fe_3C to cementite was obtained from Figs. 7(c) and 7(a), as well as the transition between η-carbide and cementite from Figs. 7(e) and 7(a). Furthermore, because the precipitates in this study undergo structural transitions in the presence of an interface with different phases, the interface energy contributes to the transformation barrier. Therefore, in this study, energy calculations of the transformation barrier for structures with two-phase interfaces were also performed. However, an attempt to reproduce the crystal structure of the precipitate accurately, including all three-dimensional interfaces, would require a structural model beyond the size that is available for first-principles calculations. Therefore, based on the experimental knowledge for habit plane,[29,34] structural models with interfaces only on the habit plane, as shown in **Fig. 8**, were created and used in the calculation. These structural models have an interface on the habit plane, but have no interface in the horizontal axial direction because of the periodic boundary condition.

The interface models were constructed using MedeA.[36] The NEB method was then applied to calculate the transition energies as in the calculations for the single phase. A

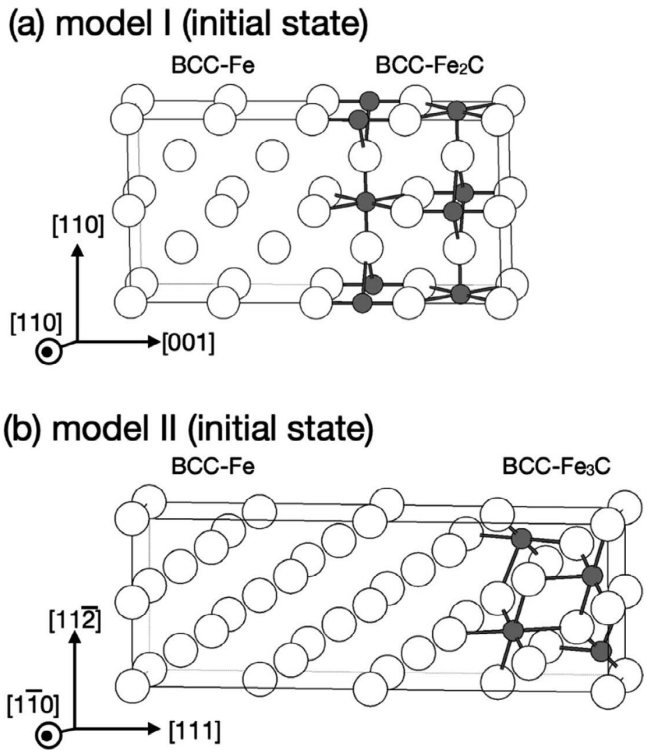

Fig. 8. Example for the initial structure models with an interface. Models I and II correspond to that listed in Table 1.

summary of the transition model with the interface is shown in **Table 1**. In this study, the process of precipitation and growth of carbides was described by a rather simplified model considering the initial and final states of the process. For example, model I corresponds to the process in which BCC produces η-Fe_2C, forming a new interface with BCC.

Table 1. List of created transition models with interfaces and transformation explanation for each model.

Model	Initial state	Final state	Explanation of transformation	Energy barrier (eV)
I	BCC-Fe/BCC-Fe_2C 6(b)/6(c)	BCC-Fe/η-Fe_2C 6(b)/6(a)	Precipitation of η-carbide in BCC matrix	0.000
II	BCC-Fe/BCC-Fe_3C 7(b)/7(c)	BCC-Fe/θ-Fe_3C 7(b)/7(a)	Precipitation of cementite in BCC matrix	0.093
III	η-Fe_2C/BCC-Fe_3C 7(d)/7(c)	η-Fe_2C/θ-Fe_3C 7(d)/7(a)	Precipitation of cementite with aid from η-carbide as precipitation site	0.075
IV	θ-Fe_3C/BCC-Fe_3C 7(a)/7(c)	θ-Fe_3C/θ-Fe_3C 7(a)/7(a)	Growth of cementite at the interface with BCC	0.055
V	η-Fe_2C/η-type-Fe_3C 7(d)/7(e)	η-Fe_2C/θ-Fe_3C 7(d)/7(a)	Precipitation of cementite in η-carbide	0.100
VI	θ-Fe_3C/η-type-Fe_3C 7(a)/7(e)	θ-Fe_3C/θ-Fe_3C 7(a)/7(a)	Growth of cementite at the interface with η-carbide	0.075

The figure numbers of the corresponding structures are listed together. The transition barrier energies obtained in Sec. 3 are also listed.

On the other hand, the model IV corresponds to the process where the BCC having the interface with the θ-Fe_3C transforms to θ-Fe_3C, resulting in an increase in the volume of θ-Fe_3C. Based on the above concept, six transition models (I-VI) given in the Table 1 were created.

3.3.2. Calculation Results of VC-NEB

The results for BCC-Fe_2C to η-Fe_2C, BCC-Fe_3C to cementite, and η-type-Fe_3C carbides to cementite calculated by VC-NEB are plotted in **Figs. 9**–**11**, respectively. Figures 9(a), 10(a), and 11(a) show the calculated energy changes for the case of a single-phase transition without interface. On the other hand, Figs. 9(b), 10(b)–10(d), and 11(b)–11(d) show the results for the transition processes calculated using the structural models with the interface for the items I–VI listed in Table 1. The initial and final structures in Figs. 10 and 11 were at first relaxed to the local stable state by structural relaxation. On the other hand, the unrelaxed initial structure was used in Fig. 9 because relaxing the initial structure led to a spontaneous change to the final structure comprising the absence of a locally stable structure.

The transition energy barriers estimated from the VC-NEB calculations are summarized in Table 1. We describe the transition barrier energies in more detail in the following sections.

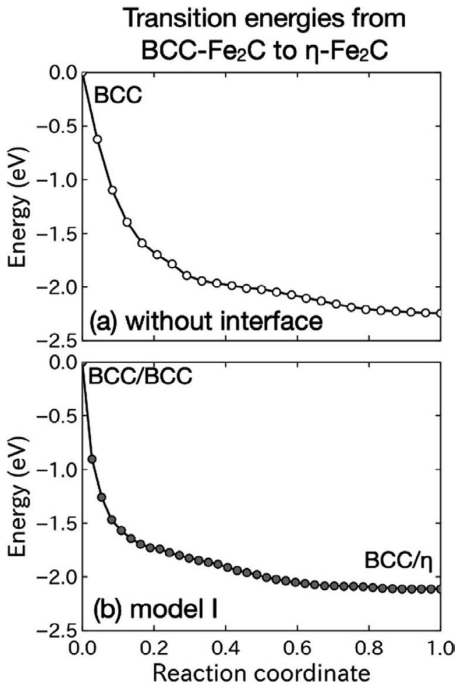

Fig. 9. Transition energies from BCC-Fe_2C to η-Fe_2C. The terms I correspond to that listed in Table 1.

3.3.3. Transitioning from BCC to η-Fe_2C

As shown in Fig. 9, transitioning from the BCC-Fe_2C to the η-carbide phase shows a monotonous and continuous decrease in energy in both cases with and without the BCC matrix interface. This is because of the high similarity in carbon and iron atom positions between the η-carbide and BCC-Fe_2C as described in Section 3.2., and thus, no large migration of atoms is required. This infers that BCC undergoes the structural phase transition to η-Fe_2C without any barriers once the clusters are generated in BCC.

However, the question arises whether the structural transformation to η-Fe_2C can occur even if the cluster size is minute. The magnitude of the critical nuclear radius is not discussed in the framework of VC-NEB because VC-NEB uses a structural model with periodic boundary conditions applied in the axial direction parallel to the interface and performs calculations in which precipitates with infinite size are generated. By contrast, the balance between the surface energy of the precipitate and the driving force per unit volume of transformation gives a finite critical core radius in reality. Then, we applied the classical nucleation theory in conjunction to obtain the precipitate nucleus size of η-Fe_2C. According to the classical nucleation theory, the critical nucleation radius, r^*, and the activation energy, Δg_c, are given by

$$r^* = -\frac{2\sigma}{\Delta G_V}, \quad \text{..... (8)}$$

$$\Delta g_c = \frac{16\pi\sigma^3}{3\Delta {G_V}^2}, \quad \text{..... (9)}$$

where σ is the interface energy and ΔG_V represents the driving force per unit volume. The interfacial energy σ was obtained from a difference between the energy E_{int} in the interfacial model and the average of the energies E_{BCC} and E_η for the BCC-Fe and η-carbide phases normalized by the area of the interface

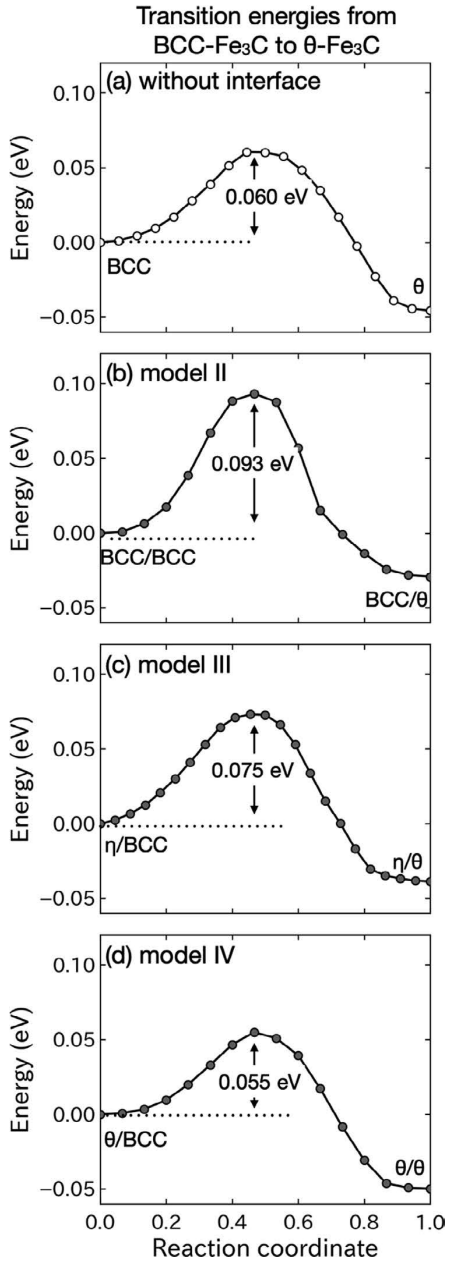

Fig. 10. Transition energies from BCC-Fe_3C to cementite. The terms II–IV correspond to those listed in Table 1. The values in the figure are the energies of the transition barriers.

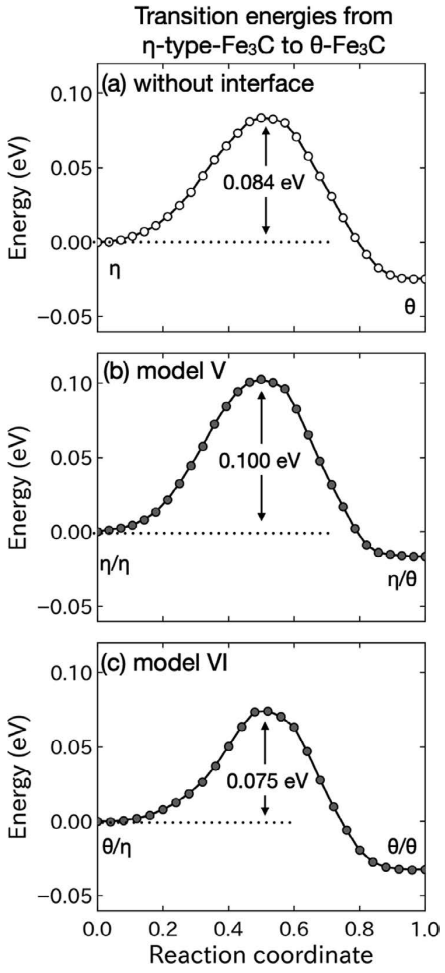

Fig. 11. Transition energies from η-type-Fe_3C to cementite. The terms V–VI correspond to those listed in Table 1. The values in the figure are the energies of the transition barriers.

Table 2. List of critical nucleation radii and activation energies.

at.%C	wt.%C	ΔG_V (kJ/m^3)	σ (J/m^2)	r^* (nm)	Δg_e (J/atom)
2.5	0.55	-2.3×10^6		0.42	3.0×10^{-20}
5.0	1.12	-2.1×10^6	0.49	0.46	3.6×10^{-20}
10.0	2.33	-1.6×10^6		0.60	6.0×10^{-20}

$$\sigma = \frac{E_{\text{int}} - \left(E_{\text{BCC}} + E_{\eta}\right)/2}{2A}. \quad \text{.....(10)}$$

The energy of each model was calculated so that the number of Fe atoms is equal. The driving force ΔG_V was calculated by calculating a tangent to the free-energy curve showing against carbon composition at the compositions of 2.5, 5.0, and 10.0 at.%C and deriving the difference between this and the tangent to the free-energy curve at the stoichiometric composition of the η-carbide phase, *i.e.*, 33 at.%C. The critical nucleation radii and activation energies calculated in this work are summarized in **Table 2**. The size of critical nucleation radii is in the order of a few atoms, and the activation energies are very small. Thus, the formation of η-carbides is considered to proceed more dominantly by the cluster formation process than by the nucleation process. Furthermore, the critical nucleation radii obtained here are consistent with previous experimental investigations[13,15] in which the precipitation of η-carbide was so fine that it was difficult to observe by electron-beam diffractometry.

3.3.4. Transition from BCC to Cementite

As shown in Fig. 10(a), the transition from BCC-Fe_3C to cementite has an energy barrier of 0.060 eV. When the interface was considered, the transition energy was 0.093 eV, as shown in Fig. 10(b). On the other hand, the energy in the case of the transition from BCC to cementite with the interface to η-carbide was calculated as 0.075 eV, given in Fig. 10(c). This value is lower than 0.093 eV, and the cementite precipitation from the BCC matrix is not likely to occur directly, but rather via precipitation with the assistance of η-carbide.

In the case of the transition of the BCC structure to cementite at the interface with cementite, the transition

barrier energy was 0.055 eV, as shown in Fig. 10(d). This energy is the smallest value among the four conditions in Fig. 10. This implies that once cementite is formed, the energy barrier for the cementite formation from the neighboring region becomes smaller and grows easily.

3.3.5. Transitioning from η-Carbide to Cementite

The transition energy from η-carbide to cementite was 0.084 eV with the absence of an interface, as shown in Fig. 11(a). The energy changed to 0.100 eV when an interface with BCC was involved, as given in Fig. 11(b). By contrast, the energy barrier for the transition of η-Fe_3C to cementite with the interface between η-Fe_2C and cementite is 0.075 eV, as shown in Fig. 11(c). Thus, it is inferred that the η-type-Fe_3C is most likely to transit to cementite under the condition that the interface with cementite exists.

4. Discussion

4.1. Clustering Behavior in BCC and BCT-Fe

The CE-CVM and Monte Carlo methods show the results of two-phase separation based on ordering. The results show that the ordered structure of BCC-Fe_2C ($P4_2/mnm$) is different from that of BCT-Fe_2C ($Pnmm$) reported previously.[20] Carbon atoms in the ordered structure occupy only the c-site in the BCT, whereas the ordered cluster is formed in the form of a- and b-site occupancy in BCC. Furthermore, the atomic arrangement of BCC is highly similar to that of η-carbide. This is the reason for the transition to η-carbide without any transition barriers besides carbon diffusion.

Recently, Kawahara *et al.*[11] identified the carbon-enriched region with a tetragonal strain of c/a = 1.1, which was inferred to be Fe_8C based on the correlation with the axial ratio of α''-$Fe_{16}N_2$. However, such a stable structure was not clarified in this study. The present study is limited to the investigation of the arrangement patterns of carbon and vacancies in the 12 sites using the maximum $Fe_4(C,Vac)_{12}$ sublattice model. A larger structural model $Fe_8(C,Vac)_{24}$ is required to describe Fe_8C; however, this calculation was avoided in the present study because of the exponentially increasing number of cluster combinations. Considering the formation of this carbide is expected to be our future research subject.

4.2. Comprehensive Transition Processes in Tempering

Transition processes are discussed from the perspective of the relationship between the clusters in BCC and the transition barrier energies. Because complex carbides such as χ-carbides and non-stoichiometric carbides such as ε-carbides are out of our scope, the discussion focuses on the carbide formation processes in the first and third stages.

4.2.1. Transition Processes in the First Stage of Tempering

The free energies calculation using the cluster expansion and variation method showed two-phase separations between Fe and Fe_2C. The Monte Carlo simulation showed that the clusters of carbon in a one-dimensional arrangement originate from the two-phase separation form in BCC-Fe. This suggests that the precipitation of η-carbide occurs almost simultaneously with the formation of clusters. Based on the classical nucleation theory, the critical nucleation radius was found to be in the order of several atoms. This result is supported by experimental findings that the initial precipitation of η-carbide occurs so finely that it is difficult to observe via electron diffraction.[13]

4.2.2. Transition Processes in the Third Stage of Tempering

Potential transitions in the third stage of tempering are discussed referring to the transition processes II, III, IV, V, and VI listed in Table 1. First, comparing the values of the energy barriers for transitions II and III, cementite is unlikely to precipitate directly from the parent phase; rather, it may precipitate on the previously formed η-carbide that acts as precipitation sites. Furthermore, because the energy barrier of transition IV is rather small, cementite grows by consuming carbon from the martensite matrix continuously. When the energy values of transitions V and VI are compared, we concluded that the transition from η-carbide to cementite begins from the interface between η-carbide and

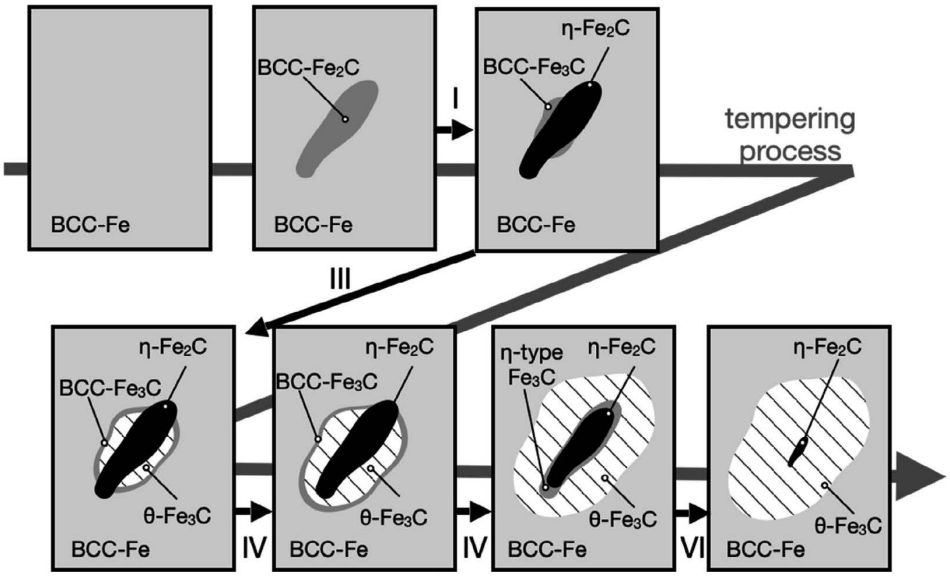

Fig. 12. Schematic diagram depicting the process of tempering in steel.

cementite produced by transition III, and eventually, the η-carbide disappears.

The whole process of tempering is summarized in the schematic diagram of **Fig. 12**. In low-temperature tempering of martensite, the transition process of "clustering" → I → III → IV → VI occurs, followed by the disappearance of metastable η-carbides via precipitation into cementite. Such a transition process is supported by previous experimental work.[13)]

5. Conclusions

In this study, the tempering behavior of martensite Fe–C was analyzed using a simulation based on first-principles calculations, and the formation mechanisms for the metastable carbides at the first and third stages of tempering were discussed. The primary findings obtained in this work can be summarized as follows:

(1) The Monte Carlo simulations using ECIs evaluated from the cluster expansion method suggested that ordered structures with a composition of Fe_2C with local structures similar to η-carbide formed in clusters in the BCC structure. Simultaneously, clusters with lower carbon concentrations were observed in the microstructure. This is caused by the two-phase separation between Fe and Fe_2C compositions calculated using the cluster expansion and variation method.

(2) The VC-NEB method showed that the transition from the BCC-Fe_2C ordered structure to η-carbide occurred, and subsequently, fine η-carbide precipitated. Furthermore, the transition from the BCC-Fe_3C ordered structure to cementite was confirmed at the interface between η-carbide and matrix in the third stage of tempering. It was suggested that the cementite formed using prior precipitated η-carbide as a precipitation site. It is possible for cementite to grow further by consuming carbon from the matrix, suggesting that η-carbides disappear through the transition to cementite.

Acknowledgments

This work was supported by JPSPS KAKENHI Grant Numbers 18H05454, 20K05058, 20H00296 and 21H01602.

REFERENCES

1) E. Matsubara, I. Tanaka, H. Ohtani, H. Yasuda, H. Numakura, T. Furuhara and S. Tsuji: Metal Organisation Studies, Asakura Shoten, Tokyo, (2011), 142 (in Japanese).
2) C. M. Wayman: Introduction to the Crystallography of Martensitic Transformations, Macmillan Series in Materials Science, New York, (1964), 1.
3) R. M. Horn: *Metall. Trans.*, **9A** (1978), 1039. https://doi.org/10.1007/BF02652208
4) S. Nagakura, Y. Hirotsu, M. Kusunoki, T. Suzuki and Y. Nakamura: *Metall. Trans. A*, **14** (1983), 1025. https://doi.org/10.1007/BF02659851
5) K. A. Taylor, L. Chang, G. B. Olson, G. D. W. Smith, M. Cohen and J. B. Vander Sande: *Metall. Trans. A*, **20** (1989), 2717. https://doi.org/10.1007/BF02670166
6) S. B. Ren, T. Tadaki, K. Shimizu and X. T. Wang: *Metall. Mater. Trans. A*, **26** (1995), 2001. https://doi.org/10.1007/BF02670672
7) Y. Nakamura and S. Nagakura: *Proc. 8th Eur. Congr. EM, Budapest*, **1** (1984), 467.
8) K. H. Jack: *J. Iron Steel Inst.*, **169** (1951), 26.
9) L. J. E. Hofer, E. M. Cohn and W. C. Peebles: *Amer. Chem. Soc.*, **71** (1949), 189. https://doi.org/10.1021/ja01169a048
10) Ph. Dünner and S. Müller: *Acta Met.*, **13** (1965), 25. https://doi.org/10.1016/0001-6160(65)90021-0
11) Y. Kawahara, K. Kaneko, H. Sawada and J. Takahashi: *Acta Mater.*, **252** (2023), 118919. https://doi.org/10.1016/j.actamat.2023.118919
12) Y. Hirotsu and S. Nagakura: *Acta Metall.*, **20** (1972), 645. https://doi.org/10.1016/0001-6160(72)90020-X
13) S. Nagakura, Y. Hirotsu, M. Kusunoki, T. Suzuki and Y. Nakamura: *Tetsu-to-Hagané*, **68** (1982), 2421 (in Japanese). https://doi.org/10.2355/tetsutohagane1955.68.16_2421
14) Y. Ohmori and I. Tamura: *Metall. Mater. Trans. A*, **23** (1992), 2737. 10.1007/BF02651753
15) M. Taniya: *Bulletin of the Japan Institute of Metals*, **11** (1972), 203 (in Japanese). https://doi.org/10.2320/materia1962.11.203
16) M. Maki: Principle and Method of Organizational Control of Steel, Uchida Rokakuho, Tokyo, (2015), 93 (in Japanese).
17) L. Morsdorf, E. Emelina, B. Gault, M. Herbig and C. C. Tasan: *Acta Mater.*, **205** (2021), 116521. https://doi.org/10.1016/j.actamat.2020.116521
18) E. C. Bain: *Trans. Amer. Inst. Min.* (*Metall.*) *Engrs.*, **70** (1924), 25.
19) Z. Nishiyama: Basic Edition of Martensitic Transformation, Maruzen, Tokyo, (1971), 11.
20) M. Enoki, Y. Osawa and H. Otani: *Tetsu-to-Hagané*, **106** (2020), 342 (in Japanese). https://doi.org/10.2355/tetsutohagane.TETSU-2019-098
21) R. Kikuchi: *Phys. Rev.*, **81** (1951), 988. https://doi.org/10.1103/PhysRev.81.988
22) G. Kresse and J. Furthmüller: *Phys. Rev. B*, **54** (1996), 11169. https://doi.org/10.1103/PhysRevB.54.11169
23) G. Kresse and J. Furthmüller: *Comput. Mater. Sci.*, **6** (1996), 15. https://doi.org/10.1016/0927-0256(96)00008-0
24) M. H. F. Sluiter, C. Colinet and A. Pasturel: *Phys. Rev. B*, **73** (2006), 174204. https://doi.org/10.1103/PhysRevB.73.174204
25) F. Murnaghan: *Proc. Nat. Acad. Sci. USA*, **30** (1944), 244. https://doi.org/10.1073/pnas.30.9.244
26) G. R. Qian, X. Dong, X.-F. Zhou, Y. Tian, A. R. Oganov and H.-T. Wang: *Comput. Phys. Commun.*, **184** (2013), 2111. https://doi.org/10.1016/j.cpc.2013.04.004
27) A. R. Oganov and C. W. Glass: *J. Chem. Phys.*, **124** (2006), 244704. https://doi.org/10.1063/1.2210932
28) A. R. Oganov, A. O. Lyakhov and M. Valle: *Acc. Chem. Res.*, **44** (2011), 227. https://doi.org/10.1021/ar1001318
29) W. Pitsch and A. Schrader: *Arch. Eisenhütt.*, **29** (1958), 715. https://doi.org/10.1002/srin.195803018
30) E. Tekin and P. M. Kelly: Precipitation from Iron-Base Alloys, Gordon and Breach Sci. Publ., New York, (1965), 208.
31) W. Pitsch: *Acta Metall.*, **10** (1962), 79. https://doi.org/10.1016/0001-6160(62)90190-6
32) N. J. Petch: *Acta Cryst.*, **6** (1953), 96. https://doi.org/10.1107/S0365110X53000260
33) I. V. Isaichev: *Z. Tekhn. Fiz.*, **17** (1947), 835.
34) A. Y. Bagaryatsky: *Dokl. Akad. Nauk. SSSR.*, **73** (1950), 1161.
35) K. Nakai and Y. Omori: *Materia Japan*, **40** (2001), 52. https://doi.org/10.2320/materia.40.52
36) MedeA 3.2, Material Design Co, San Diego, (2020).